Unsupervised Phenotyping Reveals Disrupted Neural Firing Characteristics in the Anterior Thalamus and Surrounding Brain Regions Following Third-Trimester Equivalent Alcohol Exposure in Mice

M.D. Morningstar[1], G. Acosta[2], C.F. Valenzuela[1], B.J. Clark[2], D. N. Linsenbardt[1]

1. University of New Mexico School of Medicine and Health Sciences Center, Department of Neurosciences, Albuquerque, New Mexico, 87131, United States.

2. University of New Mexico, Department of Psychology, Albuquerque, New Mexico, 87131, United States.

This work was supported in part by grant #s: AA015614, AA025120, AA007462, AA023786, AA029700, and the New Mexico Alcohol Research Center P50-AA022534, .

Abstract

Acute binge-like third-trimester-equivalent alcohol exposure (TTAE) causes apoptosic neurodegeneration in brain regions necessary for spatial learning and memory, such as the anterior thalamus (AT), which encodes context-relevant information, including head direction. While we are beginning to understand the behavioral consequences of this exposure, the neural correlates of spatial cognition deficits are underexplored. Thus, we recorded a mixture of neurons from the AT and surrounding brain regions in mice with TTAE while they freely moved within a controlled environment. To model acute binge-like TTAE, C57BL/6J mice received 2 injections of 2.5 g/kg alcohol (or saline) on post-natal day (PND) 7. Subjects were then left undisturbed until the day of surgery as adults (>PND 60), when they were implanted with silicon or multi-wire arrays. Mice were placed in a circular 40 cm diameter arena under dim red light with 2 LED cues on the walls that rotated on a pseudo-random basis while electrophysiological data was recorded. Following data preprocessing, spike and waveform features were extracted from each putative single spiking unit. These features were reduced utilizing uniform manifold approximation and projection (UMAP). Following dimensionality reduction, we used agglomerative hierarchical clustering to find populations of neurons with similar features. Following this, we compared each feature based on treatment and found the features most important to disambiguate TTAE's impact on neural activity. TTAE was associated with *decreases* in mean firing rate, peak firing rate, rebound index, and tail decay constant, *increases* in alpha, peak to trough time, and repolarization time, and bidirectional differences as a function of neuronal subtype in burst index and rebound index. This suggests that TTAE produces long-lasting and fundamental differences in spiking features that can be observed *in vivo* and are amenable to intervention. Together, this dataset provides further clarifying criteria that can be utilized to diagnose and treat FASD.

Introduction

Fetal Alcohol Spectrum Disorders (FASDs) encompass a range of neurodevelopmental abnormalities resulting from in utero alcohol exposure. These conditions are associated with lasting cognitive, behavioral, and neurological impairments, including deficits in spatial learning and memory. One particularly vulnerable developmental window is the third trimester equivalent of human pregnancy, which in rodents corresponds to the early postnatal period (Dobbing & Sands, 1979). In some regions of the United States, third-trimester alcohol exposure (TTAE) accounts for up to 8% of FASD cases (Umer et al., 2020).

Emerging evidence indicates that the hippocampal-diencephalic-cingulate (HDC) network—a brain circuit critical for spatial navigation and memory—is a key target of third-trimester-equivalent alcohol exposure (TTAE). First described by Papez and later refined through cross-species research, this circuit includes the hippocampal formation, mammillary bodies, retrosplenial cortex (RSC), and anterior thalamic nuclei (ATN) (Bubb et al., 2017; Papez, 1937; Vogt, 2019). The HDC network enables allocentric navigation, contextual learning, and the integration of spatial cues.

Within this network, neurons in the anterodorsal (AD) nucleus of the thalamus serve as head direction (HD) cells, firing in relation to an animal's orientation in space. These neurons encode directional information using both internal cues (e.g., vestibular, proprioceptive, and motor signals) and external landmarks (Clark & Harvey, 2016; Taube, 2007). Their activity is shaped by inhibitory input from the thalamic reticular nucleus (TRN) and modulated by reciprocal connections with the RSC and hippocampus (Clark et al., 2010; Roy et al., 2021; Vantomme et al., 2020). Disruption of this circuitry through lesions to the ATN or RSC leads to impaired navigation, underscoring the importance of bidirectional thalamocortical communication in spatial cognition.

Acute, binge-like alcohol exposure on postnatal day (PND)7 in rodent models induces widespread neuronal apoptosis in components of the HDC network, including the subiculum, RSC, and ATN (Ikonomidou et al., 2000; Wozniak et al., 2004). The ATN appears particularly susceptible, with PND 7 ethanol exposure resulting in a roughly 60% reduction in AD volume in rodents (Ikonomidou et al., 2000), and similar damage reported in non-human primates (Farber et al., 2010). In humans, prenatal alcohol exposure has been linked to thalamic volume loss and reduced activation during spatial memory tasks (Harvey et al., 2019; Woods et al., 2018). Additional rodent studies show long-term morphological changes in thalamocortical pathways and sex-dependent alterations in functional connectivity (Granato et al., 1995; Rodriguez et al., 2016). The AD nucleus, in particular, shows functional impairments following TTAE, including decreased intrinsic excitability, diminished excitatory postsynaptic currents in RSC-projecting AD neurons (Bird et al., 2023) and reduced Fos expression following contextual learning (Morningstar et al., 2025), suggesting broad circuit-level dysfunction.

Despite well-documented anatomical and molecular disruptions following acute binge-like TTAE, its functional impact on ATN activity during behavior remains poorly understood, particularly in awake, freely moving animals. We hypothesized that acute TTAE produces long-lasting alterations in the functional properties of ATN neurons in ways that can be detected *in vivo* during naturalistic behavior. To test this, we used high-density electrophysiological recordings to examine neural activity in and around the ATN of behaving mice, sampling over 1,500 neurons across multiple thalamic depths. We applied unsupervised phenotyping, using uniform manifold approximation and projection (UMAP) and agglomerative hierarchical clustering, to identify distinct neuronal subpopulations based on waveform and spiking features, and to assess whether these subpopulations differ between treatment groups. We show that this approach provides a critical link between *ex vivo* observations and *in vivo* function, offering

a more comprehensive understanding of how developmental alcohol exposure impairs real-time circuit dynamics underlying spatial cognition.

Methods

Animals

All animal procedures were approved by the UNM-HSC Animal Care and Use Committee and adhered to NIH guidelines. C57BL/6J breeding pairs were obtained from Jackson Labs and maintained on a 12-h reverse light/dark cycle (lights on at 8 p.m.) in a dedicated colony room. Animals' were kept in micro-isolated systems with ventilated lid tops and cages (Lab Products, Seaford, DE). All animals had *ad libitum* access to water and rodent chow (Teklad 2920x, Envigo, Indianapolis, IN) and water.

Treatment

On PND 7, mice were subcutaneously injected twice with saline or ethanol (20% v/v in normal saline) at a dose of 2.5 g/kg spaced 2 hours apart, which results in peak blood ethanol concentrations (BECs) nearing 400 and 500 mg/dL (Wozniak et al., 2004). All treatments were performed on a per litter basis such that all mice in a given litter received saline or alcohol. Mice were returned to their litter until weaning on PND 20 and allowed to age at least until PND 60 (**Figure 1A**).

Surgery

On the day of surgery, adult mice were pulled from group housing and isolated. Isoflurane induction was done at 500 mL/min at a concentration of 2% (SomnoFlo; PhysioSuite; RightTemp, Kent Scientific, Torrington, CT). Following cessation of motor response, mice were pulled from the induction chamber and placed into the stereotaxic instrument (Kopf, Germany). Upon successfully moving the mice over to the nose cone, flow rate was reduced to 250 mL/min

at the same concentration of 2% and raised up to 2.3% as needed. Following cessation of spinal reflexes, a circular incision was performed to reveal skull. A combination of scraping and hydrogen peroxide cleared the skull surface until bregma and lambda were readily visible. Coordinates for bregma were taken and the skull was leveled with reference to lambda. A rectangular craniotomy was performed medial to the AD (AP: 0.651, ML: 1.085, DV -3; Sunkin et al., 2013; **Figure 1B**). OptiBond (Kerr, USA) was applied to the skull surface and treated with blue light. Probes attached to 3D printed moveable microdrives were then lowered at a 12-12.5-degree angle. Silicon elastomers (DuraGel, CambridgeNeurotech, UK; Kwik-Sil, WPI, USA) were applied to the open craniotomy to protect underlying tissue. Additional 3D printable hardware was implanted to the skull to protect the electrode.

Data acquisition and apparatus

All hardware was controlled using Bonsai. All electrophysiology data was acquired utilizing an OpenEphys Acquisition Board (OpenEphys, Atlanta). A Chameleon3 FLIR (Teledyne FLIR, UK) camera collected high-resolution video at 40 FPS. LED cues were controlled using custom Arduino software and output TTLs on every event. Animals were placed inside a 36.83 cm diameter cylinder with gray walls. Affixed to the gray walls was either a stationary cue card or 4 8x8 LED arrays arranged in 90-degree intervals. At any given time, only 2 of the 4 LED lights were active and displayed a blue X or green ^ across the full 8x8 array (similar to Duszkiewicz et al., 2024). LED arrays were pseudorandomly swapped on a roughly 10-minute inter-trial interval. All data were collected at 20 kHz and at broadband (1 – 6,000 Hz; **Figure 1C**).

Data preprocessing

Data were spike-sorted using a combination of SpikeInterface (Buccino et al., 2020) and Kilosort4 (Pachitariu et al., 2024). Data were curated in MATLAB2023b (MathWorks, Natick, MA) using quantitative spiking metrics, such as refractory violations and the distribution of

amplitudes. Videos were preprocessed in DeepLabCut (Mathis et al., 2018) and exported as CSV files. Broadband signals were downsampled to 1250 Hz for any LFP analyses.

Feature curation and dimensionality reduction

10 features were extracted from the waveforms and spike times of our single-units. From the waveforms, we assessed the peak-to-through duration and time to repolarization using similar methods as those previously published (Ardid et al., 2015; Morningstar et al., 2020). The spiking features utilized were the following: mean interspike interval (ISI), mean firing rate, coefficient of variation (C_v), the parameters alpha and beta obtained from fitting a gamma distribution to the distribution of ISIs, burstiness, maximum firing rate, and the variance of the firing rate (**Figure 1D**). These 10 features were combined into a single matrix that was normalized between [0 1], log-transformed, and then reduced using UMAP. Using the reduction from UMAP, hierarchical agglomerative clustering was performed with complete linkage in order to produce meaningfully separated clusters based on the reduced feature space (**Figure 1E**). At 30% of the resulting dendrogram, this resulted in 12 unique clusters.

Statistics

Data was assessed for normality and log-transformed as appropriate. Generally, the features utilized were non-normally distributed but achieved normality after log transformation. Following data transformation, two-tailed t-tests were performed between all pairwise combinations of treatment effects within a cluster. The resulting p-values were then FDR corrected with alpha set to 0.05.

Random forest classification was also employed to determine the impact of the features used on predicting outcomes, such as cluster identity or treatment. We utilized an out-of-bag error classifier to determine which features produce the greatest jump in error when omitted from the predictor.

Results

Spike and waveform features were computed and reduced through UMAP resulting in a reduced feature space that was subsequently clustered with hierarchical agglomerative clustering (**Figure 2A**). Next, the relative importance of each feature utilized in our UMAP reduction was determined by utilizing a random forest classifier to predict cluster identity based on how much error emerges when that feature is left out of the classifier. Therefore, large values indicate a particular feature's absence caused a large amount of error in the classifier. In our clustering, we see that the burstiness of the cell and peak to through time have the two most prominent peaks in relative importance (**Figure 2B**). Next, we assessed how our neurons were dispersed across each cluster as a function of treatment. Qualitatively we observe that the overall magnitude of neurons differs across each cluster, however, the relative proportion is the same (**Figure 2C**). Next, in a manner similar to the above random forest classifier, we sought to determine if any specific feature predicted treatment, and none had prominent peaks (**Figure 2D**). Following this, we assessed the raw number of neurons per cluster belonging to each treatment group. Again, the raw magnitudes are significantly different across each cluster and treatment group ($\chi^2 = 34.17$, $p < 0.001$; **Figure 2E**). However, when normalized by each treatment's total number of neurons, we see that the proportion of neurons belonging to each cluster is not significantly different ($\chi^2 = 0.075$, $p = 1$) suggesting that each treatment has a similarly sampled population of neurons.

The distribution of individual features was overlaid on the UMAP reduction and clusters wherein large values are represented by warmer colors, small values are represented by cooler colors. First, we assessed the mean ISI which shows a gradient distribution across each cluster with clusters 3 and 7 having some of the largest values (**Figure 3A**). The CV was also assessed and it appeared to have gradients both globally and locally within clusters (**Figure 3B**). Burstiness demonstrated a smaller global gradient as well as limited local gradient (**Figure 3C**).

Following mapping the features to our UMAP space, we assessed whether each feature within a cluster showed significant differences between treatment effects. All comparisons were done utilizing FDR-corrected t-tests within a cluster. From this, we saw no significant differences in either the mean ISI or CV as a function of treatment (**Figure 3D,E**). A significant treatment difference was observed in the burstiness of neurons belonging to cluster 7 (**Figure 3F**).

The same analysis was conducted for all other features. Next, we observed a similar global gradient in the mean firing rate along the x-axis (**Figure 4A**) as well as within the maximum firing rate and variance of the firing rate along the x and y-axis (**Figure 4B,C**). Each feature was assessed for significant treatment differences. A significant difference in the mean firing rate was observed for cluster 2 (**Figure 4D**). A significant difference in the maximum firing rate was observed for both cluster 4 and cluster 7 (**Figure 4E**). No significant differences were observed in the variance of the firing rate (**Figure 4F**). Next, we assessed the parameters obtained by fitting a gamma distribution to the ISI distribution. In general, alpha is related to the height of the ISI distribution while beta is related to the width of the ISI distribution. There was no obvious gradient for our alpha value (**Figure 5A**), however, we did see a gradient predominately along the x-axis for our beta value (**Figure 5B**). Interestingly cluster 7, which saw significant differences in burstiness as well as maximum firing rate, is where the largest beta values exist within our UMAP reduction space. We assessed if there were treatment differences and saw a significant difference in alpha within cluster 7 (**Figure 5C**) and there were no significant differences across any clusters for beta (**Figure 5D**).

Next, waveform properties were assessed across the UMAP reduction space as well as within each treatment. No clear gradients were observed for either the repolarization time or peak to through time beyond a small dip in values along the origin of the y-axis (**Figure 6A,B**). The mean waveforms for each treatment and cluster were plotted with individual traces behind them (**Figure 6C**). Treatment effects for each cluster were assessed. Significant differences

between treatments were observed in repolarization time for cluster 2, 9, 10, and 11 (**Figure 6D**). Significant differences were also observed between treatments for the peak to through time for clusters 9 and clusters 11 (**Figure 6E**). 3-dimensional autocorrelograms (3D-ACGs) were calculated with code adapted from (Yu et al., 2024). Briefly, these represent the probability of a spike occurring across an individual neuron's deciled firing rate. This is important because across our 2hr sessions, a single neuron may exhibit multiple modes and rates of activity that may be lost in an overall mean. 3D-ACGs were averaged within each cluster and interpolated to form representative 3D-ACGs for each cluster and treatment (**Figure 7A**). 3D-ACGs were quantified at the individual level with 3 metrics: the burst index, rebound index, and tail decay constant. Significant treatment differences within cluster 7 and cluster 9 were found in both the burst and rebound indices (**Figure 7B-C**). Clusters 1, 5, 6, 8, 9, and 11 showed significant treatment differences in the tail decay constant (**Figure 7D**).

Last, all FDR corrected p-values are listed for each feature and cluster (**Figure 8A**). White squares highlight significant features within a cluster. Importantly, the effect size was also calculated with Cohen's d (**Figure 8B**). Again, white squares highlight significant features within a cluster. Last, the sum of the absolute value of Cohen's d was calculated for each feature across the varying clusters (**Figure 8C**). This value highlights the features that showed the greatest effect sizes between treatment conditions, suggesting that they are likely the most critical features for distinguishing between saline and TTAE treatments. The top 5 features from greatest to least include tail decay constant, peak-to- trough time, burst and rebound indices, and burstiness.

Discussion

The present study first sought to determine if meaningful clusters could be detected across a heterogeneous, predominately thalamic, dataset using waveform and spiking features. Following clustering, it was then determined if meaningful treatment differences could be

detected within each cluster. Critically, this methodology enables an unbiased approach to identifying the most important spike and waveform features that TTAE may alter by comparing neurons with similar functional features. We ultimately found several significant differences between saline and TTAE treated animals within our clusters. Following this, effect sizes were calculated for each feature tested and an overall, composite Cohen's d was determined for each feature. This composite Cohen's d suggests that the top 5 most critically changed features occurring from TTAE are the tail decay constant, peak-to-trough time, rebound index, burst index, and burstiness.

Currently there are few studies that have investigated the effects of developmental alcohol exposure using *in vivo* electrophysiology, particularly with a focus on TTAE and the relationship between TTAE and/or thalamic function. However, we can instead make inferences based on existing *ex vivo* and histological datasets. For example, several papers have shown widespread markers of apoptosis in the AT and brain regions related to the murine anterior thalamus following TTAE (Bird et al., 2023; Smiley et al., 2023; Wozniak et al., 2004) with certain models of TTAE resulting in up to a 60% reduction in the anterodorsal thalamus' (AD) volume (Smiley et al., 2023). Decreases in AT volume have also been observed in clinical populations (Treit et al., 2013). Additionally, it has been observed that neurons that project to the retrosplenial cortex from the AD show a significant reduction in excitability and spontaneous postsynaptic currents following TTAE vapor models (Bird et al., 2023). Critically, these studies have all been accomplished using *ex vivo* preparations; thus it is unknown how intact circuitry of the AT and related structures may behave following TTAE.

Other studies have employed in-depth phenotyping of AT electrophysiological features and have found distinct differences between AD and anteroventral (AV) properties. While both AV and AD contain spatially tuned neurons that discharge as a function of an animal's HD, called HD cells (Clark & Taube, 2012; Taube, 2007). The AV has a significant population of

theta-modulated (4-12Hz) HD cells, whereas the AD is largely comprised of HD cells that are not theta-modulated (Tsanov, Chah, Vann, et al., 2011; Tsanov, Chah, Wright, et al., 2011). These cells were broken down into HD cells and HD modulated by theta (HD-theta) cells, and it was observed that the HD-theta cells show a significantly shorter ISI compared to their HD, likely AD, counterparts (Tsanov, Chah, Vann, et al., 2011). This suggests that the behavioral correlates as well as basic firing characteristics such as ISI, and likely other related features, meaningfully separate the electrophysiological properties of the AT.

A key feature of interest that showed significant differences between treatment groups, specifically in the putative AD cluster, was burstiness. Thalamic cells show a high degree of bursting onto cortical cells, likely as a mechanism for regulating perceptual and attentional processes, and have been observed across multiple species and thalamic nuclei (Lesica & Stanley, 2004; Swadlow & Gusev, 2001). One mechanism that regulates thalamic bursting is known as the hyperpolarization current, or I_h, which Kulkarni et al., (2011) hypothesized was responsible for their observation of single-cell persistent activity in the AD following the application of sequences of hyperpolarizing pulses. Furthermore, recent work has shown that the gene that encodes one receptor subtype responsible for the I_h current, *Hcn1,* is highly and differentially expressed in the AD relative to its neighboring thalamic subnuclei (Kapustina et al., 2024). These findings combined with the fact that burstiness was only impacted in the putatively AD cluster we identified, the HCN1 channel may be responsible for driving treatment effects observed within that cluster. To date, no research has specifically looked at the functional role of *Hcn1* in the AD following developmental alcohol exposure; however, some research suggests it may mediate alcohol preference and intake in a developmentally specific manner (Salling & Harrison, 2020; Yao et al., 2023). *Hcn1* also has a functional role in giant depolarizing potentials (GDPs) observed during development within hippocampal sections (Bender et al., 2005), and GDP activity is increased by acute alcohol during the third-trimester, which suggests it may play

a causal role in the damaging effects of TTAE (Galindo et al., 2005; Galindo & Valenzuela, 2006). However, these excitatory effects were not observed in vivo, where alcohol has a depressant impact on network activity activated by sensory input (Lebedeva et al., 2017). These data collectively suggest that HCN1 channel function may underlie TTAE-induced alterations in spatial cognition, but further investigation will be required.

Additional impacted features, such as the decay constant, burst and rebound indices, and the peak-to-trough duration, are all related to both the intrinsic and network level excitability of a neuron. For all of these features, except the peak-to-trough duration, we see decreases indicating that less coordinated, temporally correlated spiking activity is occurring. In combination with the increase in peak to through duration, it appears that several of these clusters are showing decreases in excitability similar to what has been observed *ex vivo* (Bird et al., 2023). Deficits in neuronal excitability could subsequently lead to difficulties in stabilizing neuronal representations, such as place cells. Indeed, we see deficits in hippocampal place cell firing as well as theta rhythmicity that may be related to the neuron's excitability (Harvey et al., 2020). The clinical impacts of these decreases in excitability may include deficits in spatial cognition observed in children with FASD (Dodge et al., 2020; Willoughby et al., 2008). Therefore, understanding how TTAE and other developmental exposures impacts neuronal excitability is critical towards developing treatments.

Several future directions could extend the work presented here. First, by utilizing the critical features identified in this dataset, machine learning techniques can be employed to predict with high confidence whether a subject received saline or TTAE treatments in test datasets. The present study specifically focused on how the properties of individual neurons, *in vivo*, may be altered by TTAE. A critical next step will be to focus on how these individual properties manifest in network-level differences. For example, and as discussed above, deficits in excitability likely lead to deficits in place cell formation (Harvey et al., 2020). Additionally, it is

likely that the tuning features of HD cells may be similarly impacted by TTAE. Understanding how these features scale to local field potentials and electroencephalographs could aid in clinical evaluations of humans suspected to have FASD. Last, finding therapeutic targets to restore key features to control levels may subsequently aid in developing treatments for some of the cognitive deficits observed in those with FASD.

The present study also has several key limitations worth highlighting. First, there is no ground truth in this dataset. Therefore, whereas clusters exist and have meaningfully separable differences, the identities of those clusters are unknowable without additional information. Previous studies have paired optogenetics with *in vivo* electrophysiology to isolate genetically defined subpopulations of neurons, which can serve as ground truth datasets (Beau et al., 2025), a strategy we could adopt in future studies. Another caveat to our approach is that it is difficult to know the degree to which the current clusters are being generated based on anatomical location versus cell type. In lieu of this specific information, inferences can be made based on the features of a given cluster. For instance, and as mentioned above, cluster 7 has several features similar to HD cells within the AD such as a high maximum firing rate, a high beta value, and an irregularly shaped 3D-ACG. Future work will supplement the present findings by utilizing this framework to predict spatially selective neurons and subsequently test those predictions with behavioral data.

Overall, the present paper is the first to investigate the *in vivo* functional consequences of TTAE on thalamic neuronal activity. Utilizing a dimensionality reduction approach with several spike and waveform features, we found 12 unique clusters within our dataset. In those clusters, we analyzed whether treatment effects exist within each of the analyzed features. From this, we found that the tail decay value, peak-to-trough time, burst index, rebound index, and burstiness of the neurons were most significantly impacted by our acute binge-like TTAE paradigm. Thus,

TTAE leads to profound functional consequences to the thalamus that persist into adulthood and that may serve as treatment targets for FASD.

Ardid, S., Vinck, M., Kaping, D., Marquez, S., Everling, S., & Womelsdorf, T. (2015). Mapping of Functionally Characterized Cell Classes onto Canonical Circuit Operations in Primate Prefrontal Cortex. *Journal of Neuroscience*, *35*(7), 2975–2991. https://doi.org/10.1523/JNEUROSCI.2700-14.2015

Bender, R. A., Galindo, R., Mameli, M., Gonzalez-Vega, R., Valenzuela, C. F., & Baram, T. Z. (2005). Synchronized network activity in developing rat hippocampus involves regional hyperpolarization-activated cyclic nucleotide-gated (HCN) channel function. *The European Journal of Neuroscience*, *22*(10), 2669–2674. https://doi.org/10.1111/j.1460-9568.2005.04407.x

Bird, C. W., Mayfield, S. S., Lopez, K. M., Dunn, B. R., Feng, A., Roberts, B. T., Almeida, R. N., Chavez, G. J., & Valenzuela, C. F. (2023). Binge-like ethanol exposure during the brain growth spurt disrupts the function of retrosplenial cortex-projecting anterior thalamic neurons in adolescent mice. *Neuropharmacology*, *241*, 109738. https://doi.org/10.1016/j.neuropharm.2023.109738

Bubb, E. J., Kinnavane, L., & Aggleton, J. P. (2017). Hippocampal - diencephalic - cingulate networks for memory and emotion: An anatomical guide. *Brain and Neuroscience Advances*, *1*(1), 2398212817723443. https://doi.org/10.1177/2398212817723443

Buccino, A. P., Hurwitz, C. L., Garcia, S., Magland, J., Siegle, J. H., Hurwitz, R., & Hennig, M. H. (2020). SpikeInterface, a unified framework for spike sorting. *eLife*, *9*, e61834. https://doi.org/10.7554/eLife.61834

Clark, B. J., Bassett, J. P., Wang, S. S., & Taube, J. S. (2010). Impaired Head Direction Cell Representation in the Anterodorsal Thalamus after Lesions of the Retrosplenial Cortex. *The Journal of Neuroscience*, *30*(15), 5289–5302. https://doi.org/10.1523/JNEUROSCI.3380-09.2010

Clark, B. J., & Harvey, R. E. (2016). Do the anterior and lateral thalamic nuclei make distinct contributions to spatial representation and memory? *Neurobiology of Learning and Memory*, *133*, 69–78. https://doi.org/10.1016/j.nlm.2016.06.002

Clark, B. J., & Taube, J. S. (2012). Vestibular and attractor network basis of the head direction cell signal in subcortical circuits. *Frontiers in Neural Circuits*, *6*. https://doi.org/10.3389/fncir.2012.00007

Dobbing, J., & Sands, J. (1979). Comparative aspects of the brain growth spurt. *Early Human Development*, *3*(1), 79–83. https://doi.org/10.1016/0378-3782(79)90022-7

Dodge, N. C., Thomas, K. G. F., Meintjes, E. M., Molteno, C. D., Jacobson, J. L., & Jacobson, S. W. (2020). Reduced Hippocampal Volumes Partially Mediate Effects of Prenatal Alcohol Exposure on Spatial Navigation on a Virtual Water Maze Task in Children. *Alcoholism, Clinical and Experimental Research*, *44*(4), 844–855. https://doi.org/10.1111/acer.14310

Duszkiewicz, A. J., Orhan, P., Skromne Carrasco, S., Brown, E. H., Owczarek, E., Vite, G. R., Wood, E. R., & Peyrache, A. (2024). Local origin of excitatory–inhibitory tuning equivalence in a cortical network. *Nature Neuroscience*, *27*(4), 782–792. https://doi.org/10.1038/s41593-024-01588-5

Farber, N. B., Creeley, C. E., & Olney, J. W. (2010). Alcohol-induced neuroapoptosis in the fetal macaque brain. *Neurobiology of Disease*, *40*(1), 200–206. https://doi.org/10.1016/j.nbd.2010.05.025

Galindo, R., & Valenzuela, C. F. (2006). Immature hippocampal neuronal networks do not develop tolerance to the excitatory actions of ethanol. *Alcohol (Fayetteville, N.Y.)*, *40*(2), 111–118. https://doi.org/10.1016/j.alcohol.2006.11.001

Galindo, R., Zamudio, P. A., & Valenzuela, C. F. (2005). Alcohol is a potent stimulant of immature neuronal networks: Implications for fetal alcohol spectrum disorder. *Journal of Neurochemistry*, *94*(6), 1500–1511. https://doi.org/10.1111/j.1471-4159.2005.03294.x

Granato, A., Santarelli, M., Sbriccoli, A., & Minciacchi, D. (1995). Multifaceted alterations of the thalamo-cortico-thalamic loop in adult rats prenatally exposed to ethanol. *Anatomy and Embryology*, *191*(1), 11–23. https://doi.org/10.1007/BF00215293

Harvey, R. E., Berkowitz, L. E., Hamilton, D. A., & Clark, B. J. (2019). The effects of developmental alcohol exposure on the neurobiology of spatial processing. *Neuroscience and Biobehavioral Reviews*, *107*, 775–794. https://doi.org/10.1016/j.neubiorev.2019.09.018

Harvey, R. E., Berkowitz, L. E., Savage, D. D., Hamilton, D. A., & Clark, B. J. (2020). Altered Hippocampal Place Cell Representation and Theta Rhythmicity following Moderate Prenatal Alcohol Exposure. *Current Biology: CB*, *30*(18), 3556-3569.e5. https://doi.org/10.1016/j.cub.2020.06.077

Ikonomidou, C., Bittigau, P., Ishimaru, M. J., Wozniak, D. F., Koch, C., Genz, K., Price, M. T., Stefovska, V., Hörster, F., Tenkova, T., Dikranian, K., & Olney, J. W. (2000). Ethanol-induced apoptotic neurodegeneration and fetal alcohol syndrome. *Science (New York, N.Y.)*, *287*(5455), 1056–1060. https://doi.org/10.1126/science.287.5455.1056

Kapustina, M., Zhang, A. A., Tsai, J. Y. J., Bristow, B. N., Kraus, L., Sullivan, K. E., Erwin, S. R., Wang, L., Stach, T. R., Clements, J., Lemire, A. L., & Cembrowski, M. S. (2024). The cell-type-specific spatial organization of the anterior thalamic nuclei of the mouse brain. *Cell Reports*, *43*(3), 113842. https://doi.org/10.1016/j.celrep.2024.113842

Kulkarni, M., Zhang, K., & Kirkwood, A. (2011). Single-cell persistent activity in anterodorsal thalamus. *Neuroscience Letters*, *498*(3), 179–184. https://doi.org/10.1016/j.neulet.2011.02.051

Lebedeva, J., Zakharov, A., Ogievetsky, E., Minlebaeva, A., Kurbanov, R., Gerasimova, E., Sitdikova, G., & Khazipov, R. (2017). Inhibition of Cortical Activity and Apoptosis Caused by Ethanol in Neonatal Rats In Vivo. *Cerebral Cortex (New York, N.Y.: 1991)*, *27*(2), 1068–1082. https://doi.org/10.1093/cercor/bhv293

Lesica, N. A., & Stanley, G. B. (2004). Encoding of Natural Scene Movies by Tonic and Burst Spikes in the Lateral Geniculate Nucleus. *The Journal of Neuroscience*, *24*(47), 10731–10740. https://doi.org/10.1523/jneurosci.3059-04.2004

Mathis, A., Mamidanna, P., Cury, K. M., Abe, T., Murthy, V. N., Mathis, M. W., & Bethge, M. (2018). DeepLabCut: Markerless pose estimation of user-defined body parts with deep learning. *Nature Neuroscience*, *21*(9), 1281–1289. https://doi.org/10.1038/s41593-018-0209-y

Morningstar, M. D., Linsenbardt, D. N., & Lapish, C. C. (2020). Ethanol Alters Variability, But Not Rate, of Firing in Medial Prefrontal Cortex Neurons of Awake-Behaving Rats. *Alcoholism: Clinical and Experimental Research*, *44*(11), 2225–2238. https://doi.org/10.1111/acer.14463

Morningstar, M. D., Lopez, K. M., Mayfield, S. S., Almeida-Mancero, R. N., Marquez, J., Flores, A. M., Hafer, B. R., Estrada, E., Holtzman, G. A., Goranson, E. V., Reid, N. M., Aldrich, A. R., Ghatalia, D. V., Patel, J. R., Padilla, C. M., Chavez, G. J., Kelly-Roman, J., Bhakta, P. A., Valenzuela, C. F., & Linsenbardt, D. N. (2025). Connectivity of the neuronal network for contextual fear memory is disrupted in a mouse model of third-trimester binge-like ethanol exposure. *Alcohol, Clinical and Experimental Research*, *49*(2), 315–331. https://doi.org/10.1111/acer.15503

Pachitariu, M., Sridhar, S., Pennington, J., & Stringer, C. (2024). Spike sorting with Kilosort4. *Nature Methods*, *21*(5), 914–921. https://doi.org/10.1038/s41592-024-02232-7

Papez, J. W. (1937). A proposed mechanism of emotion. *Archives of Neurology & Psychiatry*, *38*, 725–743. https://doi.org/10.1001/archneurpsyc.1937.02260220069003

Rodriguez, C. I., Davies, S., Calhoun, V., Savage, D. D., & Hamilton, D. A. (2016). Moderate Prenatal Alcohol Exposure Alters Functional Connectivity in the Adult Rat Brain. *Alcoholism: Clinical and Experimental Research*, *40*(10), 2134–2146. https://doi.org/10.1111/acer.13175

Roy, D. S., Zhang, Y., Aida, T., Choi, S., Chen, Q., Hou, Y., Lea, N. E., Skaggs, K. M., Quay, J. C., Liew, M., Maisano, H., Le, V., Jones, C., Xu, J., Kong, D., Sullivan, H. A., Saunders, A., McCarroll, S. A., Wickersham, I. R., & Feng, G. (2021). Anterior thalamic dysfunction underlies cognitive deficits in a subset of neuropsychiatric disease models. *Neuron*, *109*(16), 2590-2603.e13. https://doi.org/10.1016/j.neuron.2021.06.005

Salling, M. C., & Harrison, N. L. (2020). Constitutive Genetic Deletion of Hcn1 Increases Alcohol Preference during Adolescence. *Brain Sciences*, *10*(11), 763. https://doi.org/10.3390/brainsci10110763

Smiley, J. F., Bleiwas, C., Marino, B. M., Vaddi, P., Canals-Baker, S., Wilson, D. A., & Saito, M. (2023). Estimates of total neuron number show that neonatal ethanol causes immediate and lasting neuron loss in cortical and subcortical areas. *Frontiers in Neuroscience*, *17*, 1186529. https://doi.org/10.3389/fnins.2023.1186529

Sunkin, S. M., Ng, L., Lau, C., Dolbeare, T., Gilbert, T. L., Thompson, C. L., Hawrylycz, M., & Dang, C. (2013). Allen Brain Atlas: An integrated spatio-temporal portal for exploring the central nervous system. *Nucleic Acids Research*, *41*(Database issue), D996–D1008. https://doi.org/10.1093/nar/gks1042

Swadlow, H. A., & Gusev, A. G. (2001). The impact of “bursting” thalamic impulses at a neocortical synapse. *Nature Neuroscience*, *4*(4), 402–408. https://doi.org/10.1038/86054

Taube, J. S. (2007). The head direction signal: Origins and sensory-motor integration. *Annual Review of Neuroscience*, *30*, 181–207. https://doi.org/10.1146/annurev.neuro.29.051605.112854

Treit, S., Lebel, C., Baugh, L., Rasmussen, C., Andrew, G., & Beaulieu, C. (2013). Longitudinal MRI reveals altered trajectory of brain development during childhood and adolescence in fetal alcohol spectrum disorders. *The Journal of Neuroscience: The Official Journal of the Society for Neuroscience*, *33*(24), 10098–10109. https://doi.org/10.1523/JNEUROSCI.5004-12.2013

Tsanov, M., Chah, E., Vann, S. D., Reilly, R. B., Erichsen, J. T., Aggleton, J. P., & O'Mara, S. M. (2011). Theta-Modulated Head Direction Cells in the Rat Anterior Thalamus. *Journal of Neuroscience*, *31*(26), 9489–9502. https://doi.org/10.1523/jneurosci.0353-11.2011

Tsanov, M., Chah, E., Wright, N., Vann, S. D., Reilly, R., Erichsen, J. T., Aggleton, J. P., & O'Mara, S. M. (2011). Oscillatory entrainment of thalamic neurons by theta rhythm in freely moving rats. *Journal of Neurophysiology*, *105*(1), 4–17. https://doi.org/10.1152/jn.00771.2010

Umer, A., Lilly, C., Hamilton, C., Baldwin, A., Breyel, J., Tolliver, A., Mullins, C., John, C., & Maxwell, S. (2020). Prevalence of alcohol use in late pregnancy. *Pediatric Research*, *88*(2), 312–319. https://doi.org/10.1038/s41390-019-0731-y

Vantomme, G., Rovó, Z., Cardis, R., Béard, E., Katsioudi, G., Guadagno, A., Perrenoud, V., Fernandez, L. M. J., & Lüthi, A. (2020). A Thalamic Reticular Circuit for Head Direction Cell Tuning and Spatial Navigation. *Cell Reports*, *31*(10), 107747. https://doi.org/10.1016/j.celrep.2020.107747

Vogt, B. A. (2019). Cingulate cortex in the three limbic subsystems. *Handbook of Clinical Neurology*, *166*, 39–51. https://doi.org/10.1016/B978-0-444-64196-0.00003-0

Willoughby, K. A., Sheard, E. D., Nash, K., & Rovet, J. (2008). Effects of prenatal alcohol exposure on hippocampal volume, verbal learning, and verbal and spatial recall in late childhood. *Journal of the International Neuropsychological Society: JINS*, *14*(6), 1022–1033. https://doi.org/10.1017/S1355617708081368

Woods, K. J., Thomas, K. G. F., Molteno, C. D., Jacobson, J. L., Jacobson, S. W., & Meintjes, E. M. (2018). Prenatal alcohol exposure affects brain function during place learning in a virtual environment differently in boys and girls. *Brain and Behavior*, *8*(11), e01103. https://doi.org/10.1002/brb3.1103

Wozniak, D., Hartman, R., Boyle, M., Vogt, S., Brooks, A., Tenkova, T., Young, C., Olney, J., & Muglia, L. (2004). Apoptotic neurodegeneration induced by ethanol in neonatal mice is

associated with profound learning/memory deficits in juveniles followed by progressive functional recovery in adults. *Neurobiology of Disease*, *17*(3), 403–414. https://doi.org/10.1016/j.nbd.2004.08.006

Yao, H., Wang, C., & Xia, Z. (2023). Prenatal alcohol exposure enhanced alcohol preference and susceptibility to PTSD in a sex-dependent manner through the synaptic HCN1 channel. *Journal of Affective Disorders*, *324*, 143–152. https://doi.org/10.1016/j.jad.2022.12.069

Yu, H., Lyu, H., Xu, Y., Windolf, C., Lee, E. K., Yang, F., Shelton, A. M., Winter, O., Laboratory, I. B., Dyer, E. L., Chandrasekaran, C., Steinmetz, N. A., Paninski, L., & Hurwitz, C. L. (2024, October 4). *In vivo cell-type and brain region classification via multimodal contrastive learning*. The Thirteenth International Conference on Learning Representations. https://openreview.net/forum?id=10JOlFIPjt

Figure captions

Figure 1: Schematic of methodology. **A.** Mice at post-natal day 7 were given either ethanol at 2.5 g/kg s.c. or saline; two hours were allowed to pass and a second dose of the same treatment was given. Mice were aged until at least post-natal day 60 prior to any experimentation. **B.** The anterior thalamus was targeted with recording electrodes. **C.** The mice were placed in a 40cm environment with rotating LED cues. **D.** Neurons were spikesorted and the resulting spike-and-wave features were extracted from each neuron within the dataset. Features extracted include the peak to through duration, refractory period, mean firing rate, mean ISI, C_v, burstiness, alpha, beta, maximum firing rate, and variance of the firing rate. **E.** All ten features were put into a single Nx10 matrix where N is the number of neurons. UMAP was performed to reduce dimensionality from 10D to 2D. Hierarchical agglomerative clustering was then performed to cluster the UMAP reduction.

Figure 2: **A.** UMAP reduction with corresponding cluster identities is shown. **B.** A random forest classifier was trained to determine which features are most predictive of cluster identity; burstiness and peak to through time dominated over other features. **C.** A UMAP reduction overlaid with the treatment identity of each neuron is shown. **D.** A random forest classifier was trained to determine which features are most predictive of treatment. **E.** Neuron counts per cluster and treatment were tabulated.

Figure 3. Features values were superimposed over the UMAP reduction for the (**A)** mean ISI, (**B**)**.** CV, and burstiness (**C**)**. D.** Treatment effects were assessed for the mean ISI, **E.** CV, and **F.** burstiness. A treatment effect was observed in burstiness for cluster 7.

Figure 4. Features values were superimposed over the UMAP reduction for the (**A)** mean firing rate, (**B**)**.** maximum firing rate, and variance of the firing rate (**C**)**. D.** Treatment effects were assessed for the mean firing rate, **E.** maximum firing rate, and **F.** variance of the firing rate. A treatment effect was observed in cluster 2 for the mean firing rate. A treatment effect was observed in cluster 4 and cluster 7 for the maximum firing rate.

Figure 5. Features values were superimposed over the UMAP reduction for the (**A)** alpha and **B.** beta values. **C.** Treatment effects were assessed for alpha and **D.** beta values. A significant effect was found in the alpha value for cluster 7.

Figure 6. Features values were superimposed over the UMAP reduction for the (**A)** repolarization time (**B**) and peak to through time. **C**. The normalized waveforms for voltage were plotted for each cluster and treatment. **D.** Treatment effects were assessed for the repolarization time **E.** and peak to through time. Significant treatment effects were found in cluster 9, 10, and 11 for the repolarization time. Significant treatment effects were found in cluster 9 and 11 for the peak to through time.

Figure 7. **A.** Representative 3D autocorrelograms for three clusters are shown. Features from the 3D autocorrelograms were extracted and treatment effects were assessed. **B.** The burst index was assessed; a significant treatment effect was observed in cluster 7 and cluster 9. **C.** The rebound index was assessed; a significant treatment effect was observed in cluster 7 and cluster 9. **D.** The tail decay constant was assessed; a significant treatment effect was observed in cluster 1, 5, 6, 8, 9, and 11.

Figure 8. **A.** The FDR corrected p-values for all pairwise t-test comparisons were summarized. **B.** Cohen's D was calculated. **C.** Cohen's D was summed across all clusters to generate values for each feature that summarize which features discriminate treatments.

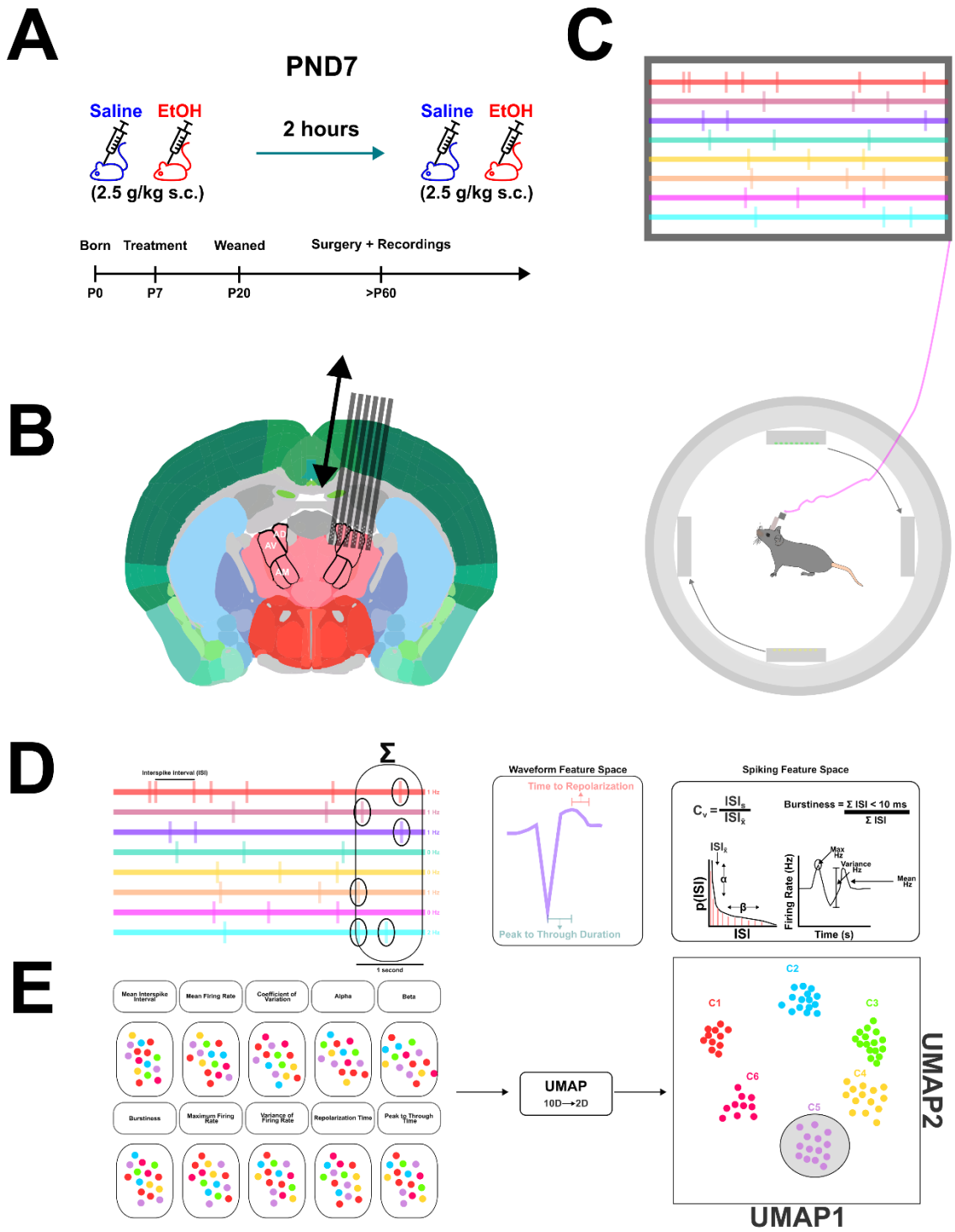
A
PND7
Saline
EtOH
(2.5 g/kg s.c.)
2 hours
Saline
EtOH
(2.5 g/kg s.c.)
Born
Treatment
Weaned
Surgery + Recordings
P0
P7
P20
>P60
B
AD
AV
AM
C
D
Σ
Interspike Interval (ISI)
1 second
Waveform Feature Space
Time to Repolarization
Peak to Through Duration
Spiking Feature Space
Burstiness = Σ ISI < 10 ms / Σ ISI
p(ISI)
ISI
Firing Rate (Hz)
Time (s)
Max Hz
Variance Hz
Mean Hz
E
Mean Interspike Interval
Mean Firing Rate
Coefficient of Variation
Alpha
Beta
Burstiness
Maximum Firing Rate
Variance of Firing Rate
Repolarization Time
Peak to Through Time
UMAP
10D→2D
C1
C2
C3
C4
C5
C6
UMAP2
UMAP1

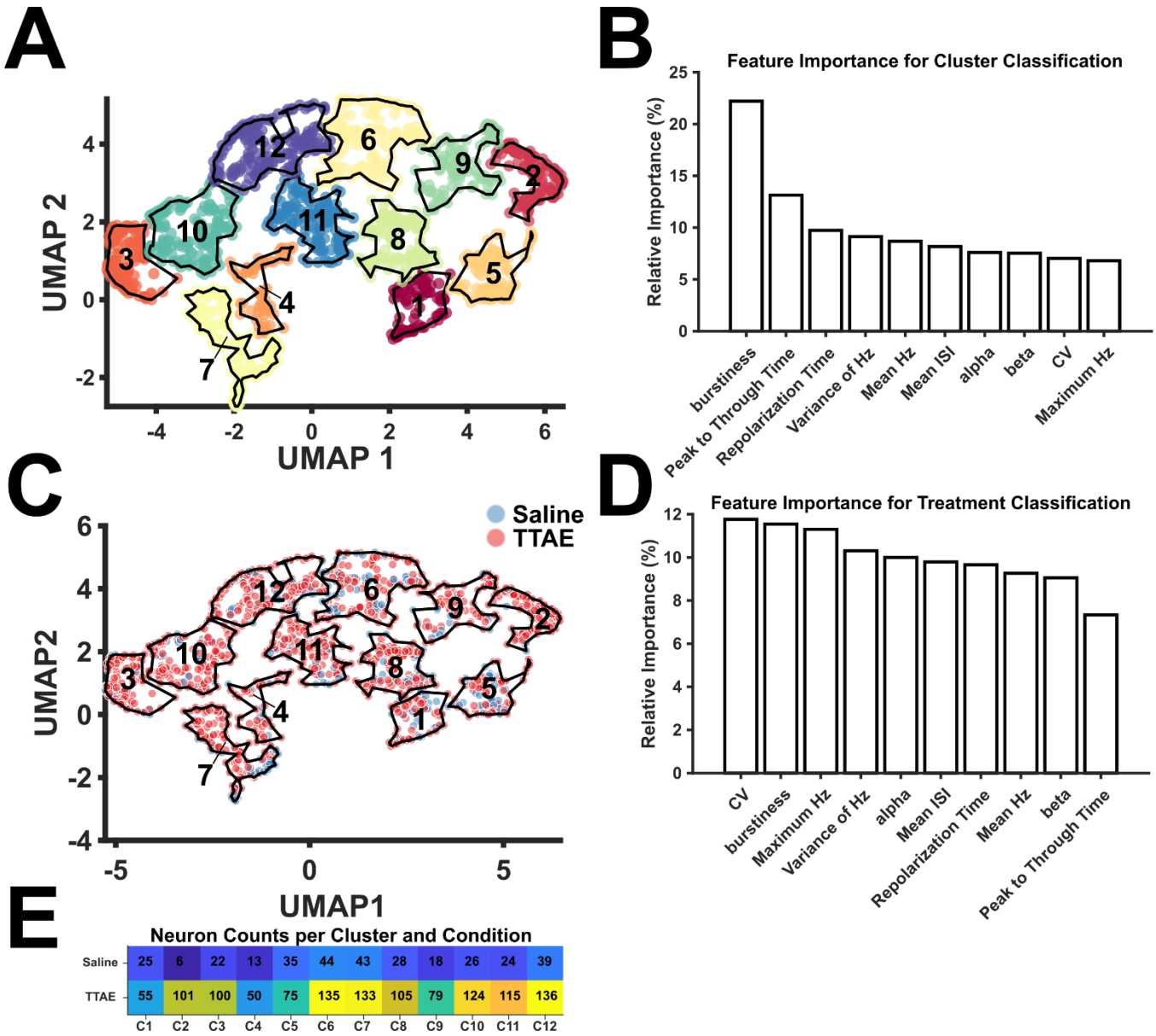
A
UMAP 2
UMAP 1
B
Feature Importance for Cluster Classification
Relative Importance (%)
burstiness
Peak to Through Time
Repolarization Time
Variance of Hz
Mean Hz
Mean ISI
alpha
beta
CV
Maximum Hz
C
Saline
TTAE
UMAP2
UMAP1
D
Feature Importance for Treatment Classification
Relative Importance (%)
CV
burstiness
Maximum Hz
Variance of Hz
alpha
Mean ISI
Repolarization Time
Mean Hz
beta
Peak to Through Time
E
Neuron Counts per Cluster and Condition
Saline 25 6 22 13 35 44 43 28 18 26 24 39
TTAE 55 101 100 50 75 135 133 105 79 124 115 136
C1 C2 C3 C4 C5 C6 C7 C8 C9 C10 C11 C12

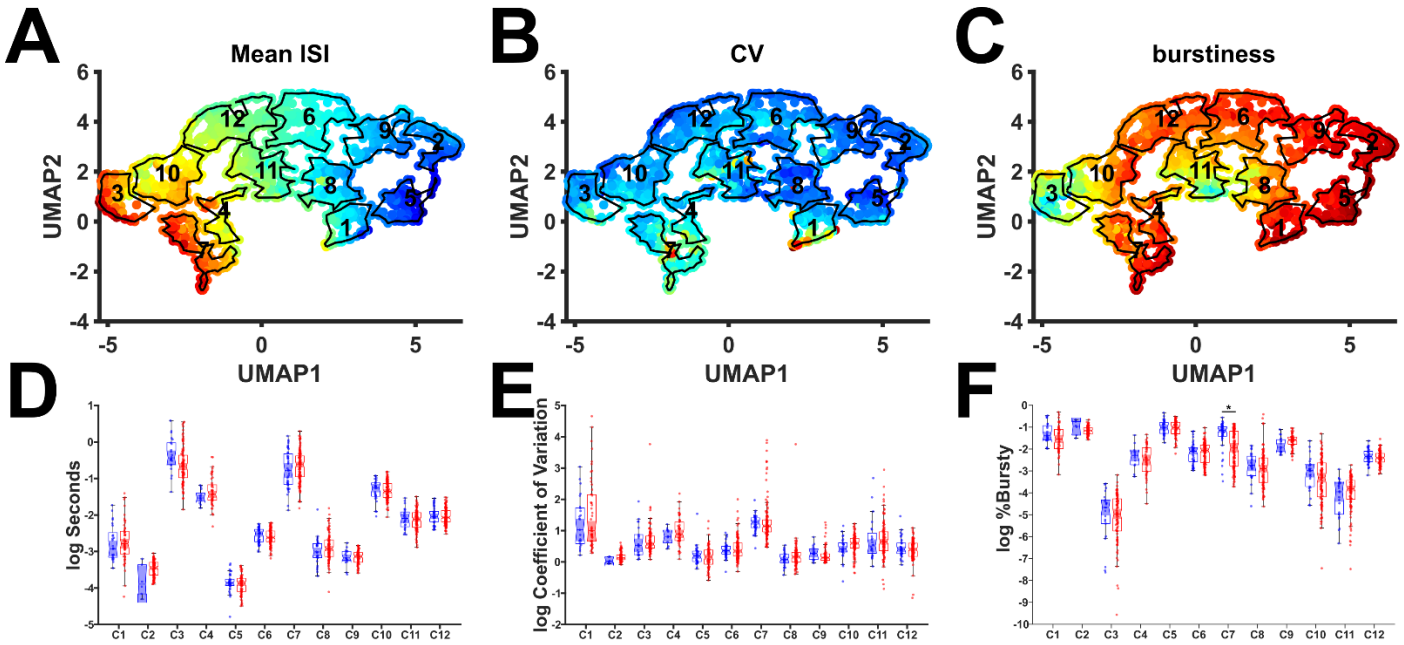
A
Mean ISI
B
CV
C
burstiness
UMAP2
UMAP1
D
log Seconds
E
log Coefficient of Variation
F
log %Bursty
C1 C2 C3 C4 C5 C6 C7 C8 C9 C10 C11 C12

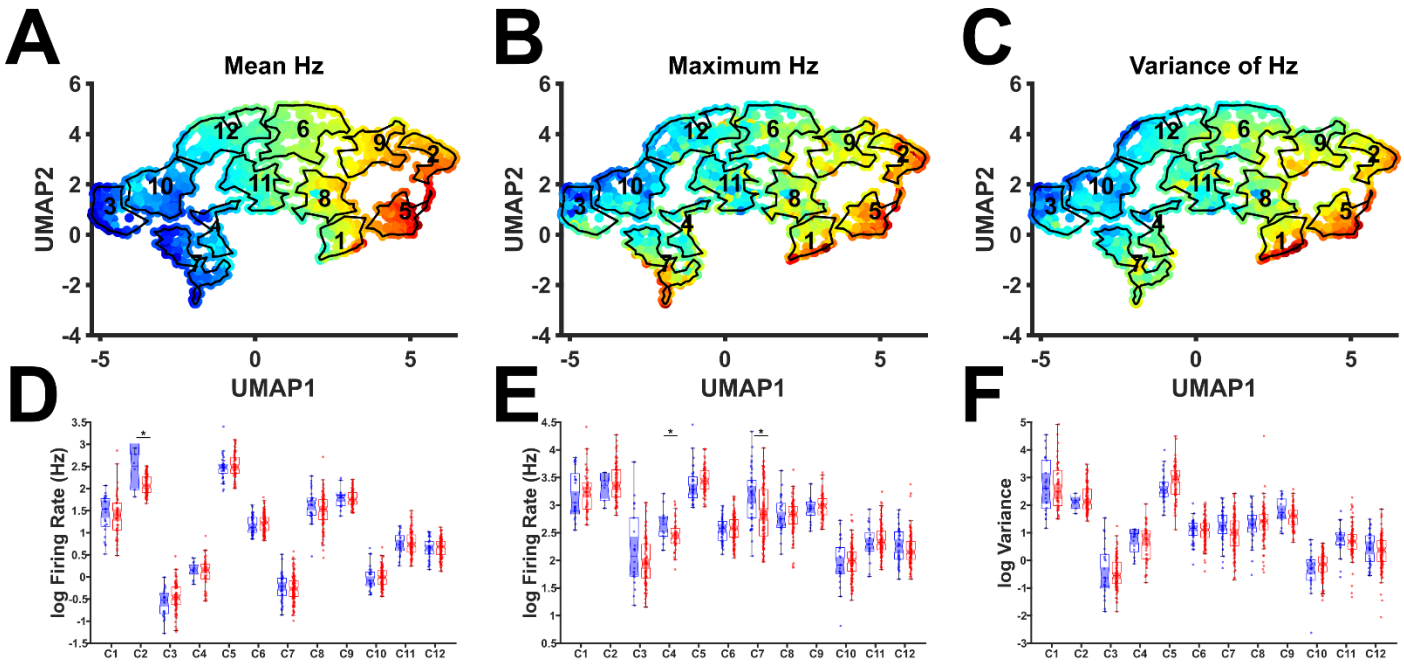
A
Mean Hz
B
Maximum Hz
C
Variance of Hz
UMAP2
UMAP1
D
E
F
log Firing Rate (Hz)
log Variance
C1
C2
C3
C4
C5
C6
C7
C8
C9
C10
C11
C12

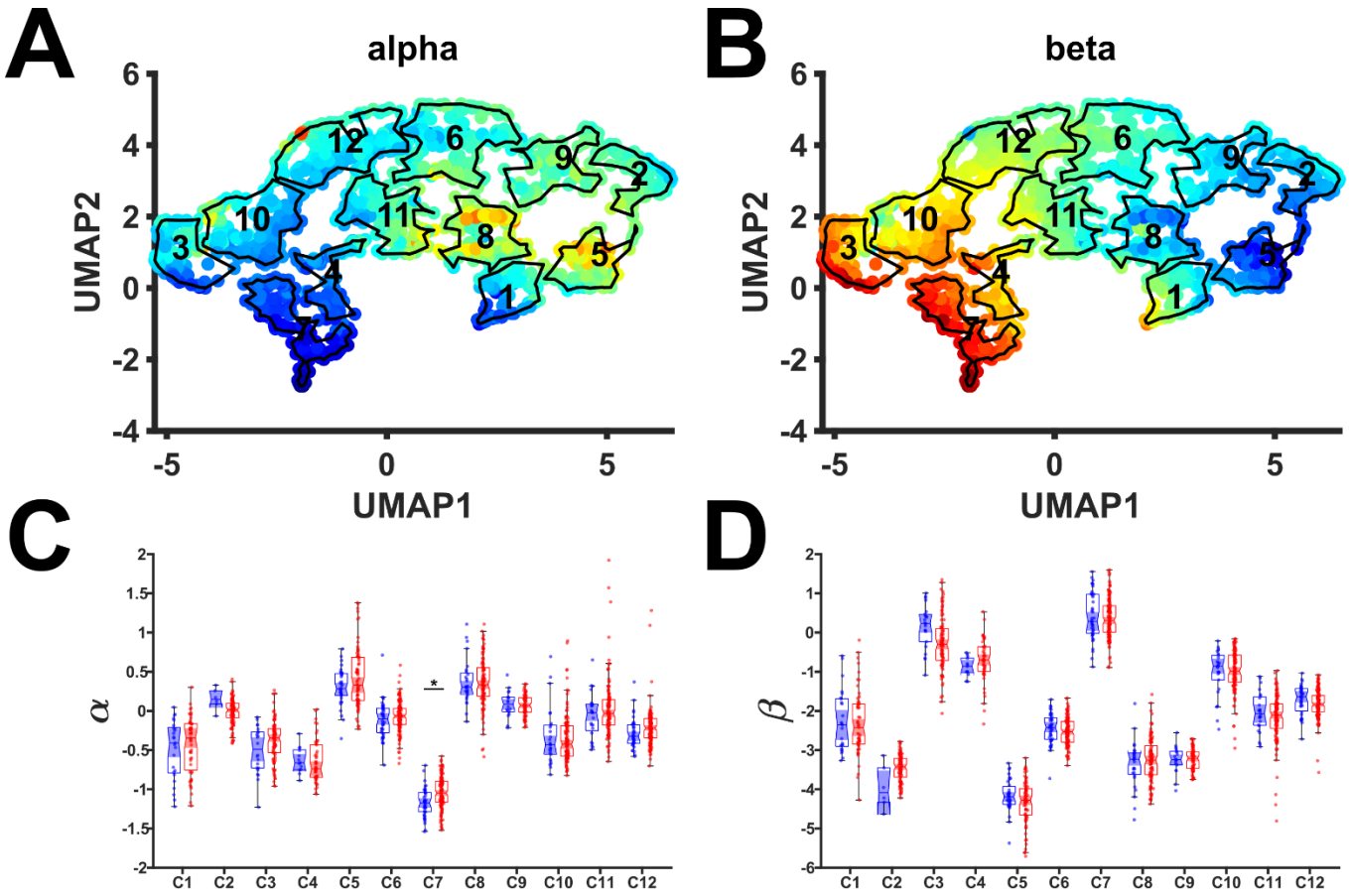
A
alpha
B
beta
UMAP2
UMAP1
1
2
3
4
5
6
7
8
9
10
11
12
C
D
α
β
C1
C2
C3
C4
C5
C6
C7
C8
C9
C10
C11
C12
*

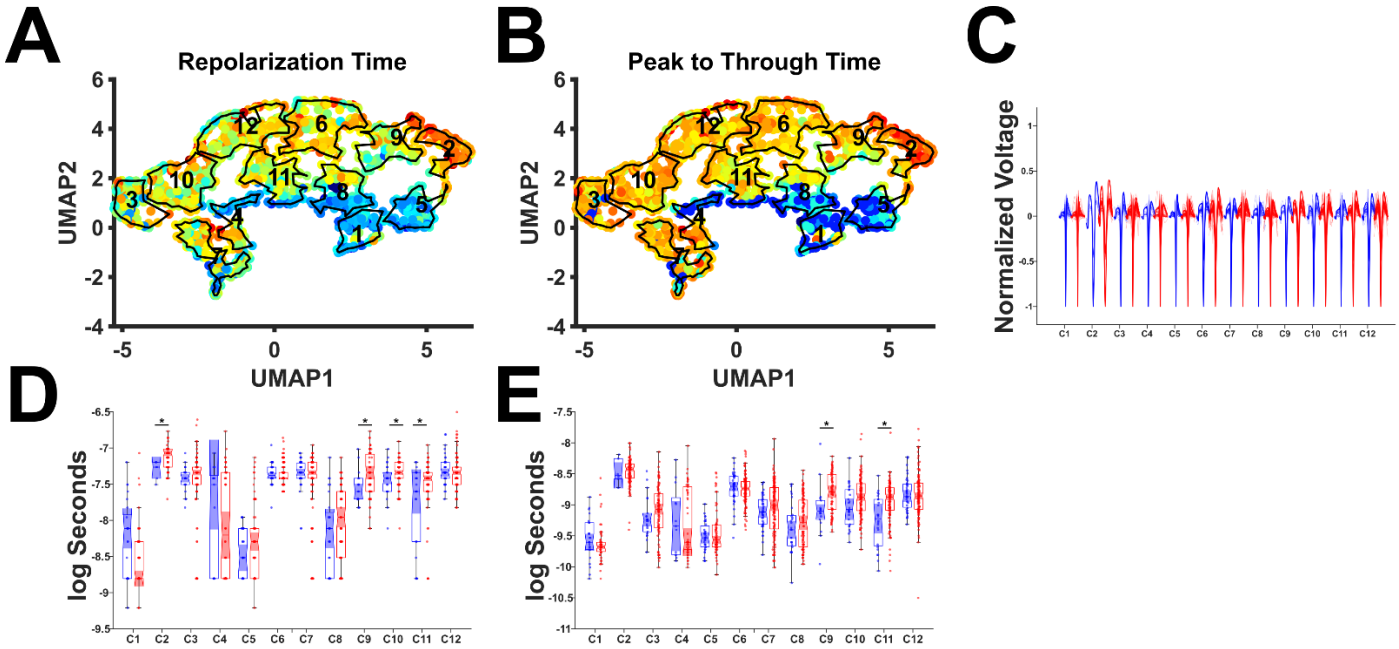
A
Repolarization Time
UMAP2
UMAP1
B
Peak to Through Time
UMAP2
UMAP1
C
Normalized Voltage
D
log Seconds
E
log Seconds
C1 C2 C3 C4 C5 C6 C7 C8 C9 C10 C11 C12

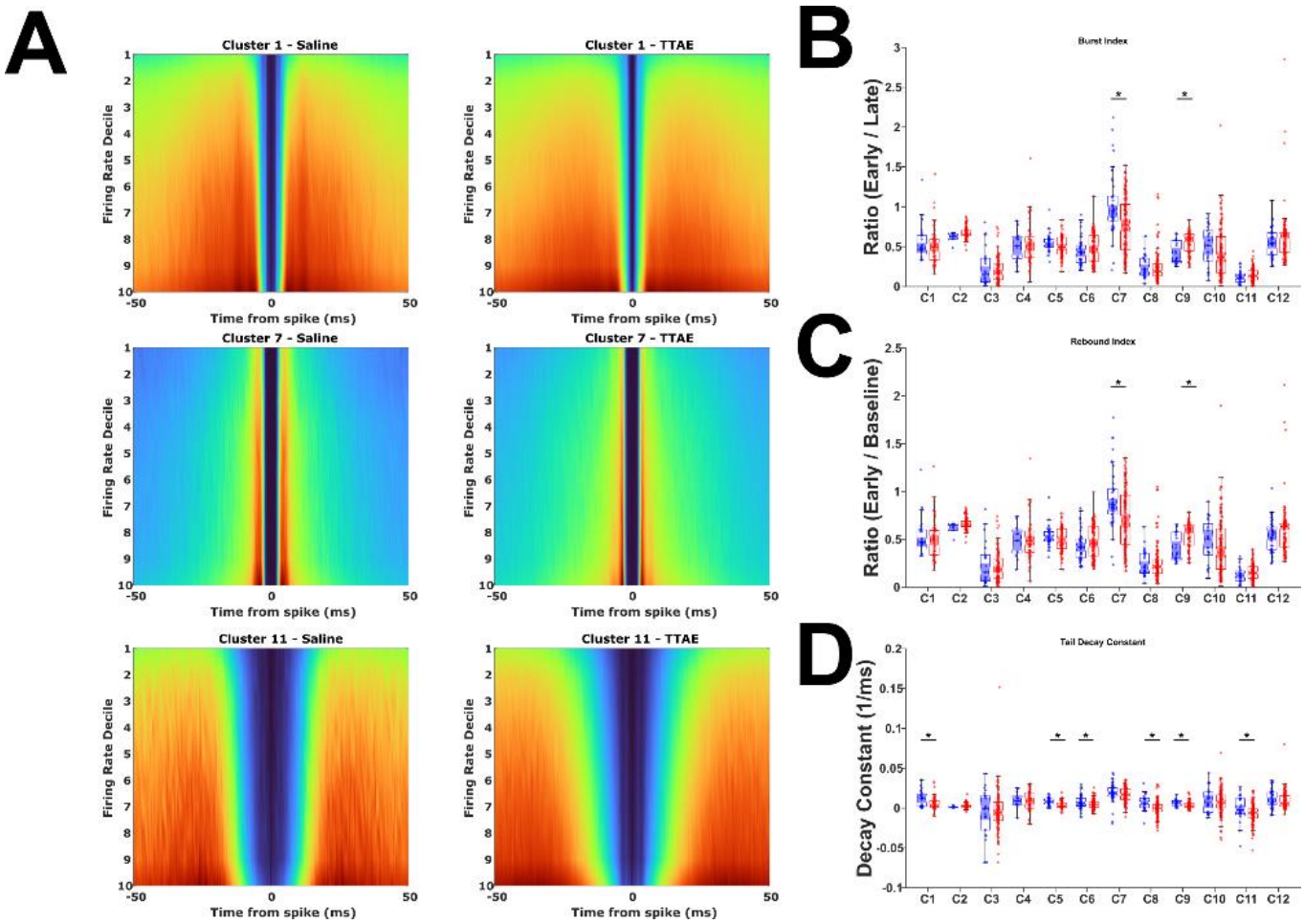
A
Cluster 1 - Saline
Cluster 1 - TTAE
Cluster 7 - Saline
Cluster 7 - TTAE
Cluster 11 - Saline
Cluster 11 - TTAE
Firing Rate Decile
Time from spike (ms)
B
Burst Index
Ratio (Early / Late)
C
Rebound Index
Ratio (Early / Baseline)
D
Tail Decay Constant
Decay Constant (1/ms)
C1 C2 C3 C4 C5 C6 C7 C8 C9 C10 C11 C12

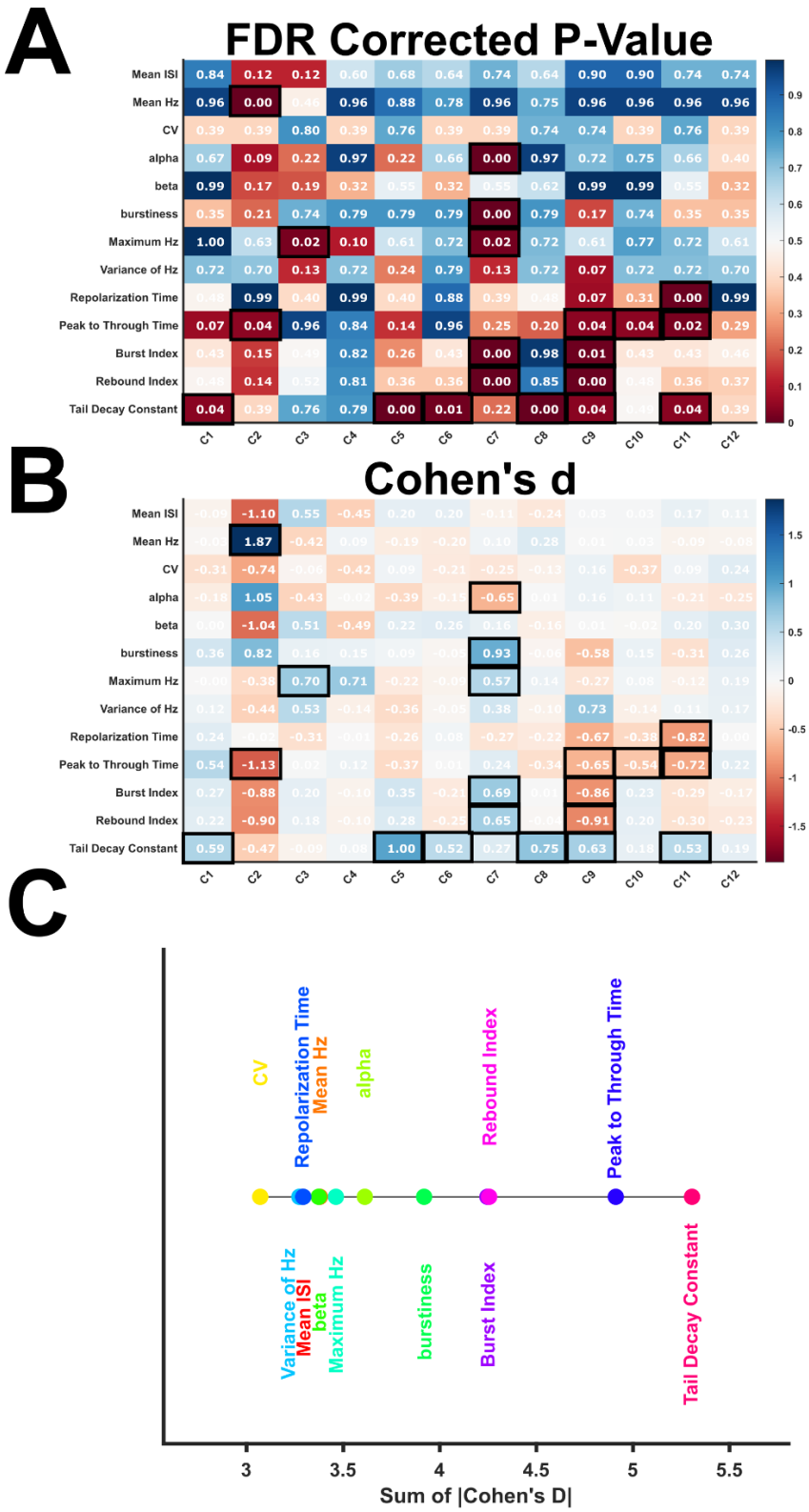
A
FDR Corrected P-Value
Mean ISI
Mean Hz
CV
alpha
beta
burstiness
Maximum Hz
Variance of Hz
Repolarization Time
Peak to Through Time
Burst Index
Rebound Index
Tail Decay Constant
C1 C2 C3 C4 C5 C6 C7 C8 C9 C10 C11 C12
B
Cohen's d
C
CV
Repolarization Time
Mean Hz
alpha
Rebound Index
Peak to Through Time
Variance of Hz
Mean ISI
beta
Maximum Hz
burstiness
Burst Index
Tail Decay Constant
3
3.5
4
4.5
5
5.5
Sum of |Cohen's D|